Journal of Manufacturing Processes 85 (2023) 503–514

Contents lists available at ScienceDirect

Journal of Manufacturing Processes

journal homepage: www.elsevier.com/locate/manpro

Physics-informed Bayesian machine learning case study: Integral blade rotors

Gregory Corson [a], Jaydeep Karandikar [b], Tony Schmitz [a,b,*]

[a] University of Tennessee, Knoxville, Mechanical, Aerospace, and Biomedical Engineering, Knoxville, TN, United States of America
[b] Oak Ridge National Laboratory, Manufacturing Science Division, Oak Ridge, TN, United States of America

ARTICLE INFO

Keywords:
Machine learning
Milling
Stability
Blisk

ABSTRACT

This paper provides a physics-informed Bayesian machine learning (PIBML) description and case study. The PIBML approach applies three physics-based models to establish the initial beliefs before testing to determine the probability of milling stability (or prior). These include: receptance coupling substructure analysis (RCSA) prediction for the tool tip frequency response functions; finite element software prediction of the mechanistic force model coefficients; and a spindle speed-dependent power law model for process damping. Testing was then performed to identify optimal stable machining conditions using an expected improvement in material removal rate criterion. The prior probability of stability was updated using the test results to determine the posterior probability of stability. The test results were compared to the parameter recommendations provided by the endmill manufacturer. A demonstration integral blade rotor was machined at the optimal stable machining conditions for 304 stainless steel and 6061-T6 aluminum. The disagreement between manufacturer recommendations and milling performance in both materials tested emphasizes the need for broad implementation of PIBML approaches to increase machining productivity and efficiency.

1. Introduction

Computer-numerically controlled (CNC) machining is projected to be a $129B industry by 2026 with 5.5 % annual growth from 2019 to 2026 [1]. It is used to produce high value components from not only plate stock, forgings, and castings, but also additively manufactured preforms. Because significant cost is already embedded in the starting material and the capital resources and hourly rates are high, it is essential that parts are not scrapped and the machine/tooling is not damaged. The production of parts that conform to design drawing specifications in a first-part-correct, high-profit scenario requires that the machining parameters, including depths of cut, spindle speed, and feed rate, as well as the material removal strategy embedded in the computer-aided manufacturing (CAM) tool path, are optimized.

While CNC machining has largely moved from an analog to a digital approach due to advances in process planning software and machine tool controllers, the selection of machining parameters remains an experience-based, trial-and-error process in many cases. This is primarily due to the large number of potential combinations for tools, holders, machines, and work materials. For example, 1000 stock keeping units (SKUs) from 50 tool providers, 500 SKUs from 50 holder manufacturers, 50 machine tool models, and 160 different metal alloys represent 1×10^{13} (or 10 million-million) different combinations. Without optimization, the outcome is reduced productivity and increased cost.

In machining, chatter (unstable machining) is caused due to the regeneration of surface waviness [2]. The information can be presented as stability maps, which separate stable and unstable combinations of axial depth of cut and spindle speed [2]. Using the stability maps, optimal stable axial depth-spindle speed pairs may be selected with the highest material removal rate. Many physics-based models are available for predicting stability, including the frequency-domain average tooth angle method [3], frequency-domain mean force approach [4], time-domain simulation [5,6], and semi-discretization method [7]. However, uncertainty in the model predictions is present due to uncertainties in the model inputs (tool tip frequency response functions, cutting force coefficients, and process damping coefficients), model assumptions, or factors that are not included in the model. Alternatively, data-driven methods can be applied to determine the stability boundary using experimental results. There have been multiple studies on the application of machine learning (ML) to machining stability. For example, Cherukuri et al. used an artificial neural network (ANN) to model

* Corresponding author at: University of Tennessee, Knoxville, Mechanical, Aerospace, and Biomedical Engineering, Knoxville, TN, United States of America.
E-mail address: tony.schmitz@utk.edu (T. Schmitz).

https://doi.org/10.1016/j.jmapro.2022.12.004
Received 14 April 2022; Received in revised form 1 November 2022; Accepted 1 December 2022
Available online 6 December 2022

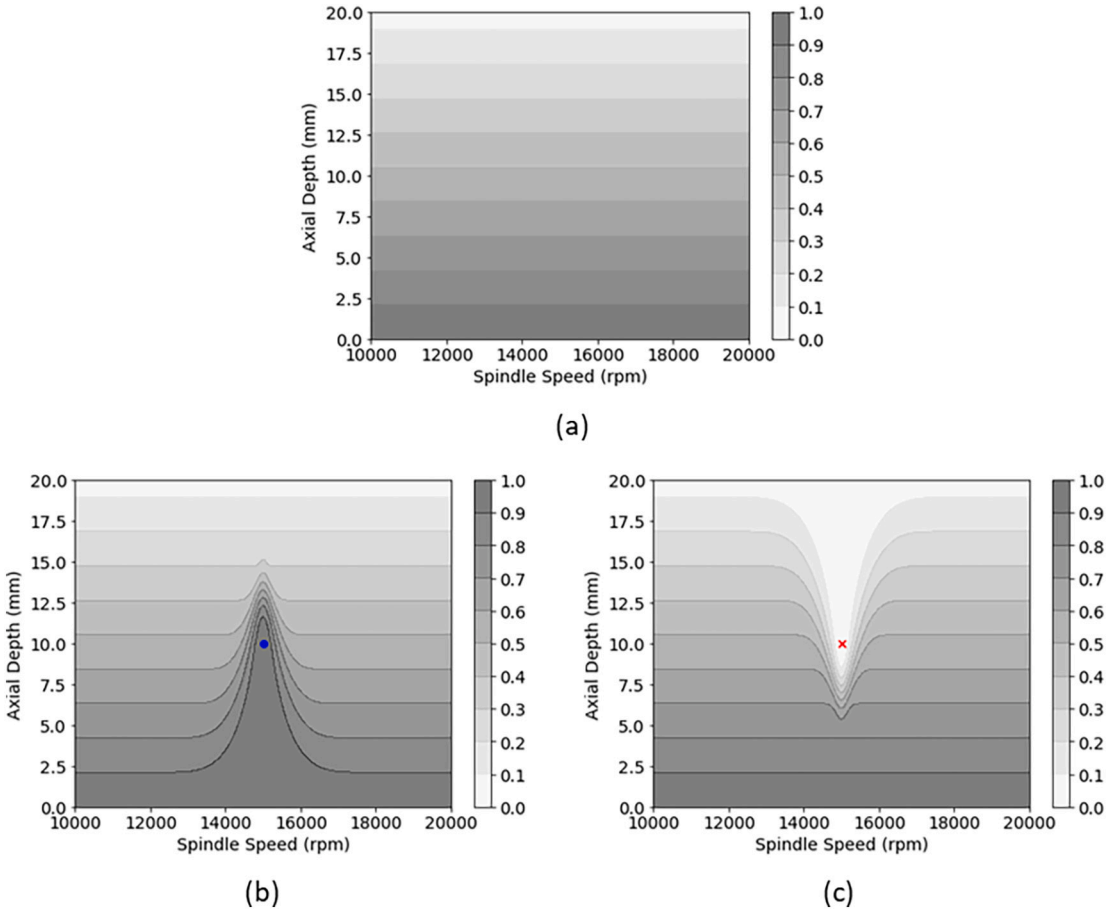

Fig. 1. (a) Prior distribution of milling stability. (b) Posterior probability of stability for a stable test at {15,000 rpm, 10 mm}. (c) Posterior probability of stability for an unstable test at {15,000 rpm, 10 mm} [14]. (For interpretation of the references to color in this figure, the reader is referred to the web version of this article.)

turning stability [8]. Denkena et al. applied support vector machines and ANNs [9]. Bergmann and Reimer implemented Regularized Kernel Interpolation for a learning stability lobe diagram to enable autonomous online parameter optimization [10]. Data-driven methods, such as ANNs, generally require many data points to accurately learn the stability boundary, do not provide information on the underlying tool tip frequency response function (FRF) and cutting force model, and may identify local, rather than global, optimized parameters [11]. Bayesian ML methods, on the other hand, enable updating the initial probabilistic stability boundary (or the prior) with each cutting test. However, recent Bayesian ML efforts [12–16] have still required significant data because the priors have not been defined based on physics-based models.

Previous work from the authors described a Bayesian learning method to update the probability of stability given test results [14]. However, the method did not use the stability model to define the prior probability of stability, but instead only applied the knowledge that it is more likely to observe an unstable cut at higher axial depths of cut. To advance the state of the art, this paper presents a systematic approach for including various process uncertainties through modeling. It builds on the approach in [14] by describing a method to define an informed prior using physics-based models to establish the initial stability beliefs.

The case study presented here addresses existing industry challenges using a combination of physics-based models, machine learning, and in-process data to provide physics-informed Bayesian machine learning (PIBML) that improves the accuracy of stability model predictions over traditional machine learning or physics-based methods individually. The application is integral blade rotors (IBRs), or blisks, machined from wrought aluminum and stainless steel prismatic stock. The machine learning approach builds on recent efforts for applying data-driven artificial intelligence to machining operations. The remainder of the paper is organized as follows. In Section 2, the Bayesian learning methodology described in [14] is shown, followed by a description of the improved method to define an informed prior using physics-based models. Section 3 describes the experimental setup and results for IBR machining. Section 4 compares updating results using informed and uninformed priors. Conclusions are provided in Section 5.

2. Modeling

2.1. Bayesian machine learning

Bayesian machine learning (BML) defines a probabilistic model of the milling stability map given test results (stable or unstable) over a spindle speed-axial depth of cut domain. Eq. (1) shows Bayes' rule for updating the probability of stability at a selected spindle speed-axial depth combination using the stability result from a test point [14].

$$p(s_g|r_t) = \frac{p(r_t|s_g)p(s_g)}{p(r_t)} \tag{1}$$

In Eq. (1), p denotes probability, s denotes stability, r denotes the test result, and subscript g and t denote a selected and test point combination of spindle speed and axial depth, respectively. A test result at t can either be stable or unstable. From Bayes' rule, the posterior probability of stability at g given the test result at t is the product of the prior probability of stability at g, and the likelihood probability of the experimental result given g is stable, divided by the marginal probability of the result.

The prior probability of stability is determined using all available information (e.g., analytical models, theoretical constraints, stability

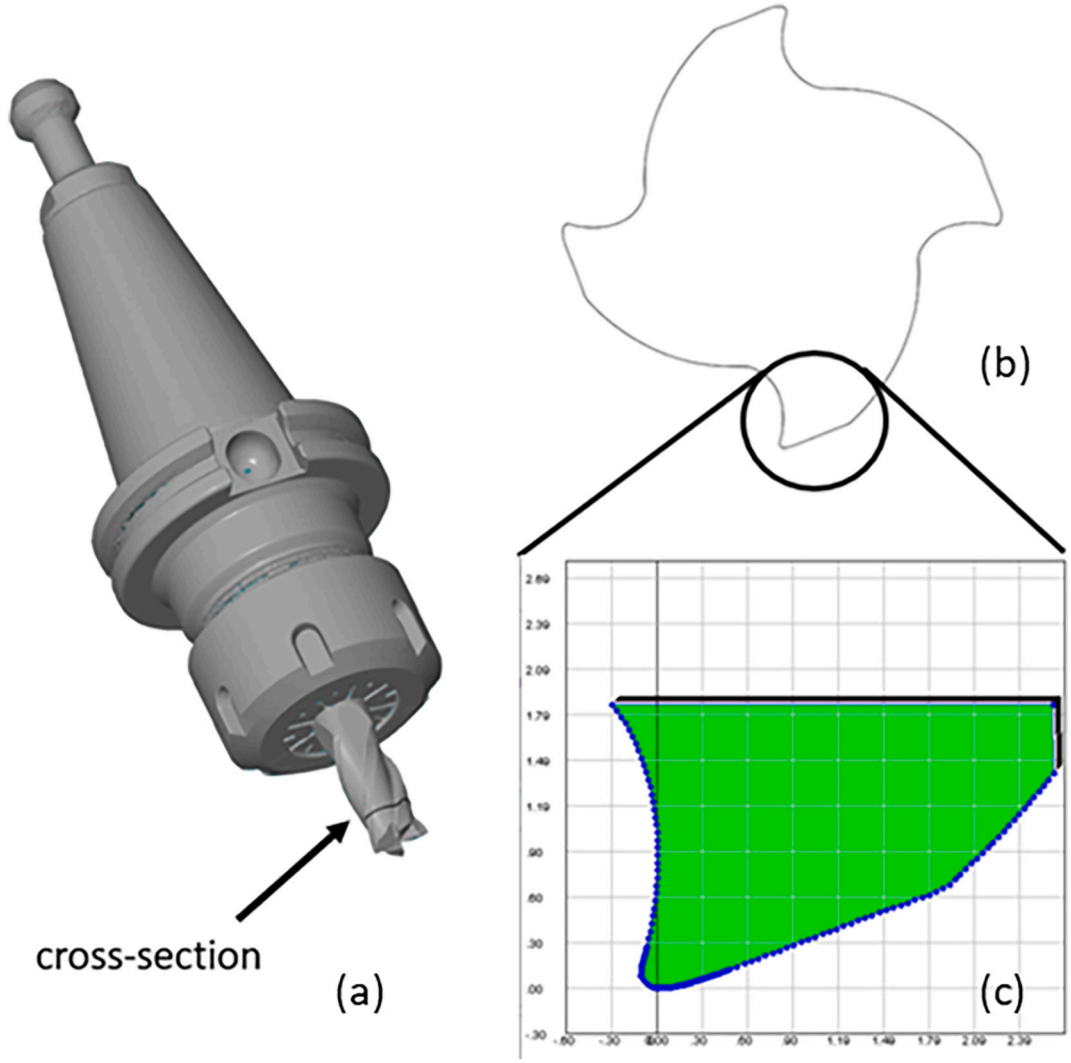

Fig. 2. (a) Tool scan using GOM ATOS Q scanner. (b) Tool edge cross-section. (c) Tool cutting edge imported in AdvantEdge™.

knowledge, and/or user experience). Fig. 1 illustrates the BML approach described in [14]. Fig. 1(a) displays the prior (or the initial probability of stability), which assumes that the probability of stability (shown in greyscale) reduces with an increasing axial depth of cut; white is likely to be unstable/chatter, while black is likely to be stable. In Fig. 1(a), the reduction in probability of stability with axial depth is linear. The prior is updated using experimental data, where the outcome is binary: the cut is labeled as either stable or unstable. The binary label is automatically assigned using the frequency content of the milling sound (obtained using a microphone), where the content at frequencies other than the tooth passing frequency and its multiples indicate chatter [2]. When the chatter peak is 50 % or higher than the tooth passing frequency peak, the cut is considered unstable (chatter).

The test result is used to update the prior using Bayes' rule to determine the posterior probability of stability (Eq. (1)) [14]. To illustrate, consider a test at {15,000 rpm, 10 mm}. Fig. 1(b) shows the updated probability of stability if the test at {15,000 rpm, 10 mm} was stable (denoted by a blue dot). Fig. 1(c) shows the updated probability of stability if the test at {15,000 rpm, 10 mm} was unstable (denoted by a red cross). As seen in Fig. 1, a stable or unstable experimental result modifies the probability of stability over the entire spindle speed-axial depth domain. This is achieved by capturing how knowledge of the stability limit at a single point affects the stability knowledge at other locations [14]. The reader is referred to [14] for the mathematical details of the BML procedure. Note that the selected test point at {15,000 rpm, 10 mm} is for illustrative purposes only.

The test parameters for stability can be selected to identify the optimal stable combination of spindle speed and axial depth using a minimum number of tests. One criterion is to test where the expected improvement in material removal rate, *MRR*, is maximum. The expected improvement in *MRR* at a selected spindle speed-axial depth combination is given by Eq. (2).

$$\mathbb{E}[I(MRR)]_g = p(s_g) \times \frac{(MRR_g - MRR_{prior})}{MRR_{prior}} \tag{2}$$

In Eq. (2), $\mathbb{E}$ denotes the expected value, I denotes improvement, the subscript g denotes an arbitrary grid point at a spindle speed-axial depth combination, MRR_{prior} is the optimal *MRR* based on the prior probability of stability, and MRR_g denotes the *MRR* at the grid point. MRR_{prior} is determined as the highest *MRR* among parameters that are stable with certainty in the domain. Results show that using the maximum expected improvement in *MRR* strategy, the optimal stable parameter can be determined in 10 to 15 tests [14].

To advance the approach described in [14], an informed prior that uses physics-based models to establish the initial stability beliefs is described here, unlike the uninformed prior in Fig. 1(a). Two primary inputs are required for the frequency-domain milling stability solution [2,3]. These include a cutting force model that relates the milling parameters to the cutting force components [2] and the tool tip FRFs that

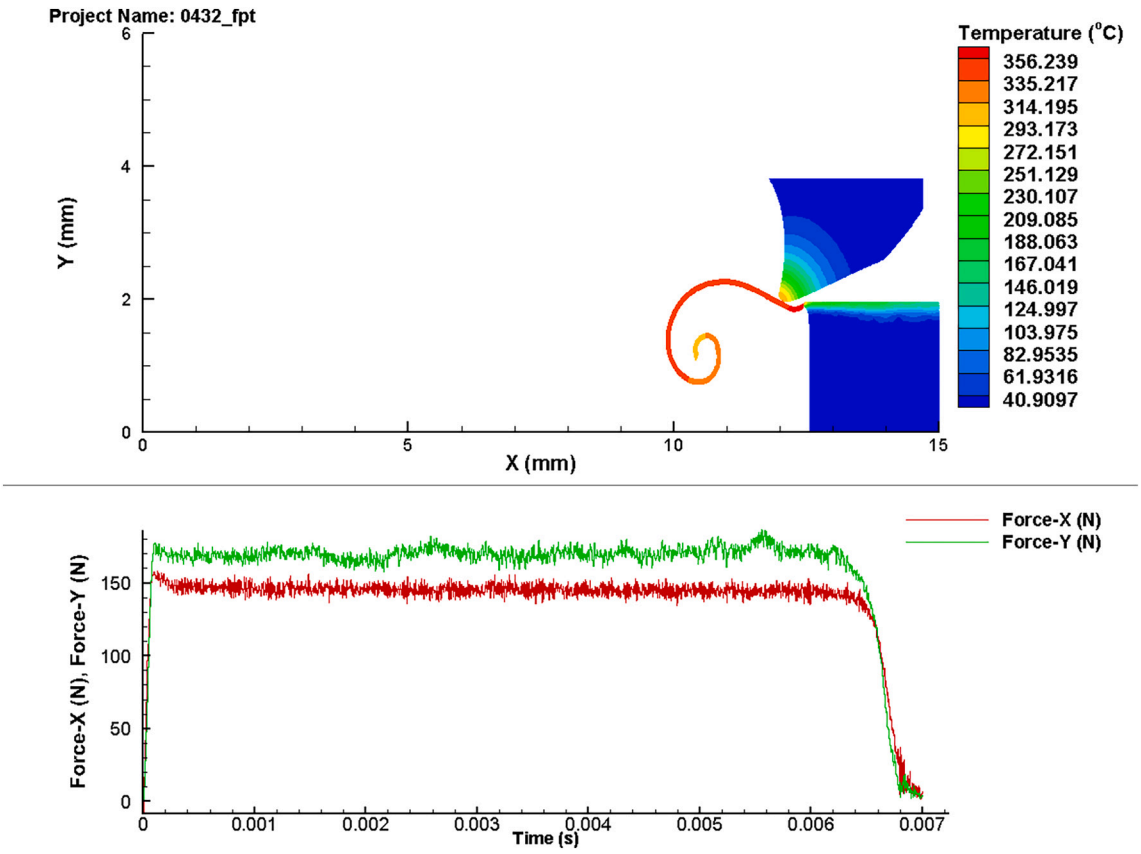

Fig. 3. Orthogonal turning simulation using AdvantEdge™.

Table 1
Cutting coefficients for mechanistic force models.

Material	Coefficients			
	k_{tc} (N/mm^2)	k_{nc} (N/mm^2)	k_{te} (N/mm)	k_{ne} (N/mm)
304 stainless steel	1618	792	138	76
6061-T6 aluminum	556	225	41	19

describes the vibration behavior of the tool-holder-spindle-machine assembly selected for the milling process [17,18]. Additionally, process damping is incorporated using a spindle speed-dependent power law model. These models and inputs are described in the following three sections. An informed prior results in an improved prior, which reduces the number of experiments required to identify the optimal stable parameters.

2.2. Finite element force modeling for cutting force coefficients

As noted, one of the primary inputs to the stability model is the cutting force coefficients [2]. The cutting force coefficients depend on the tool-material combination and may be determined using a linear regression to the mean force values measured over a range of feed per tooth values [2,3]. In this paper, a digital method to determine the cutting force coefficients using finite element simulations is presented. The commercially-available, finite element software AdvantEdge™ from Third Wave Systems was used to model the cutting force [19]. The procedure is as follows. First, the cutting tool was scanned using a GOM ATOS Q structured light scanner; the scan was used to obtain the cutting edge cross-section. Second, the cross-section was imported into the AdvantEdge™ software. Third, orthogonal cutting was simulated for a fixed chip width, b, and variable chip thickness, h. Fourth, the mean forces in the x-direction and y-direction were recorded from the finite element simulations at different chip thickness values and used to calculate the force coefficients by the linear regression method [2,3].

For 304 stainless steel, a 12.7 mm diameter endmill with four teeth and a 0.38 mm corner radius was selected. Fig. 2(a) shows the scanned tool model. Fig. 2(b) shows the tool edge cross-section. The tool edge cross-section was imported in AdvantEdge™ as shown in Fig. 2(c).

Orthogonal simulations were completed at different chip thickness values for 304 stainless steel and 6061-T6 aluminum. For the finite element simulations, the embedded power viscosity model from AdvantEdge™ was used. An adaptive remeshing scheme was used where the maximum element size was 0.1 mm and the minimum element size was 0.01 mm (default settings in AdvantEdge™). The top boundary and side boundary of the tool (shown highlighted in black) in Fig. 2(c) were fixed. The workpiece length was 12 mm. The depth of cut was 1 mm. Fig. 3 shows an example simulation results for 304 stainless steel at a 0.043 mm chip thickness and a cutting speed of 107.7 m/min. The cutting force values from the simulation were taken as the average value in the steady-state portion of the cut. In Fig. 3, the x-direction force gives the tangential force component and the y-direction force gives the normal force component.

For the simulations, the cutting speed for 304 stainless steel was 107.7 m/min. Five simulations were completed at chip thickness values of {0.023, 0.028, 0.033, 0.038, and 0.043} mm. A linear regression was then performed for the chip thickness versus mean force to identify the slope and intercept values [2,3]. These values provided the mechanistic force model coefficients in Eqs. (3) and (4), where the slopes provided the cutting coefficients (c subscripts) and the intercepts provided the edge coefficients (e subscripts).

$$F_t = k_{tc} bh + k_{te} b \tag{3}$$

$$F_n = k_{nc} bh + k_{ne} b \tag{4}$$

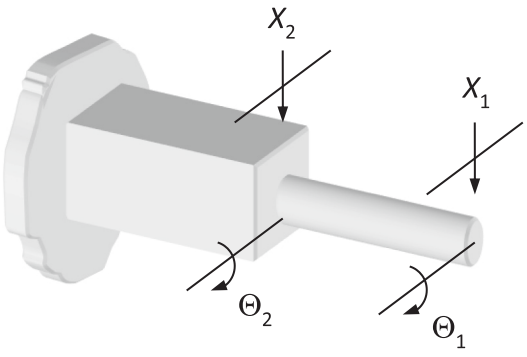

Fig. 4. RCSA example for a cylinder rigidly coupled to a prismatic cantilever beam to form an assembly.

The procedure was repeated for 6061-T6 aluminum. The tool was a 12.7 mm diameter, square endmill with three teeth. The coefficient values determined using the finite element simulation are listed in Table 1.

2.3. Process damping

Process damping is a phenomenon observed in machining where the limiting depth of cut to avoid chatter is increased at low spindle speeds (cutting speeds). Many authors have studied process damping and have described it as energy dissipation due to interference between the cutting tool clearance face and machined surface during relative vibrations between them [20–40]. There have been efforts to experimentally determine the process damping coefficients [35,36]. Budak et al. used an indentation force coefficient to identify the process damping coefficient [35]. Altinas et al. used orthogonal cutting tests with a fast servo tool to vary the phase between inner and outer modulations [36]. In this work, process damping was added using a spindle speed-dependent power law. See Eq. (5), where the increase in stability due to process damping was added to the stability boundary predicted by the frequency-domain stability solution [2,3].

$$b_{pd} = D\Omega^{d} \tag{5}$$

In Eq. (5), b_{pd} is the limiting axial depth of cut for process damping, where Ω is the spindle speed vector (rpm) and D and d are constants. The values for D and d were selected as 5×10^5 (mm/rpm) and 1.8, respectively, based on experience.

2.4. Receptance coupling substructure analysis

Receptance coupling substructure analysis (RCSA) is applied here to predict the tool tip receptance, or FRF. In the RCSA approach, a simple geometry artifact is first clamped in the spindle and measured by tap testing, where an instrumented hammer is used to excite the assembly and a low-mass accelerometer is used to measure the vibration response. Second, the spindle-machine FRF is calculated by decoupling the artifact in simulation (i.e., inverse RCSA). Third, the tool and holder models are coupled to the spindle-machine FRF to predict the tool tip FRF [17,18].

The RCSA model includes: 1) transverse deflections, x_i and X_i, for the components (lower case variables) and assembly (upper case variables) due to internal and external forces, f_j and F_j; and 2) rotations about lines perpendicular to the beam axis, θ_i and Θ_i, and bending moments (or couples), m_j and M_j, to completely describe the transverse dynamic behavior of beams. To describe the procedure, consider the cylinder-prismatic cantilever beam assembly displayed in Fig. 4. This is representative of a tool (cylinder) rigidly attached to a holder-spindle-machine (prismatic cantilever beam).

To calculate the assembly receptances, all four bending receptances are included in the component (i.e., cylinder and prismatic cantilever beam) descriptions. These four bending receptances include displacement-to-force, h_{ij}, displacement-to-couple, l_{ij}, rotation-to-force, n_{ij}, and rotation-to-couple, p_{ij}, where i is the displacement/rotation coordinate location and j is the location where the force/couple is applied. There are three primary steps followed to predict Fig. 4 assembly receptances.

1. Define the components and coordinates for the model. In this example, there are two components: a prismatic beam with fixed-free (or cantilever) boundary conditions and a cylinder with free-free (or unsupported) boundary conditions; see Fig. 5.
2. Determine the component receptances. In this work, the Timoshenko beam model was applied [41].
3. Based on the model from step 1, express the assembly receptances as a function of the component receptances from step 2. Determine the assembly receptances using the component displacements/rotations, compatibility conditions, and equilibrium conditions.

The procedure for coupling the components in Fig. 5 to form the assembly in Fig. 4 requires the component receptances. In Fig. 5, coordinates are placed at the prediction location (1) and coupling locations (2a and 2b) on the two components. For the cylinder, the direct receptances at the coordinate 1 end are shown in Eq. (6).

$$h_{11} = \frac{x_1}{f_1} \qquad l_{11} = \frac{x_1}{m_1} \qquad n_{11} = \frac{\theta_1}{f_1} \qquad p_{11} = \frac{\theta_1}{m_1} \tag{6}$$

The cross receptances are given by Eq. (7).

$$h_{12a} = \frac{x_1}{f_{2a}} \qquad l_{12a} = \frac{x_1}{m_{2a}} \qquad n_{12a} = \frac{\theta_1}{f_{2a}} \qquad p_{12a} = \frac{\theta_1}{m_{2a}} \tag{7}$$

At coordinate 2a on the cylinder, the direct and cross receptances are provided in Eqs. (8) and (9).

$$h_{2a2a} = \frac{x_{2a}}{f_{2a}} \qquad l_{2a2a} = \frac{x_{2a}}{m_{2a}} \qquad n_{2a2a} = \frac{\theta_{2a}}{f_{2a}} \qquad p_{2a2a} = \frac{\theta_{2a}}{m_{2a}} \tag{8}$$

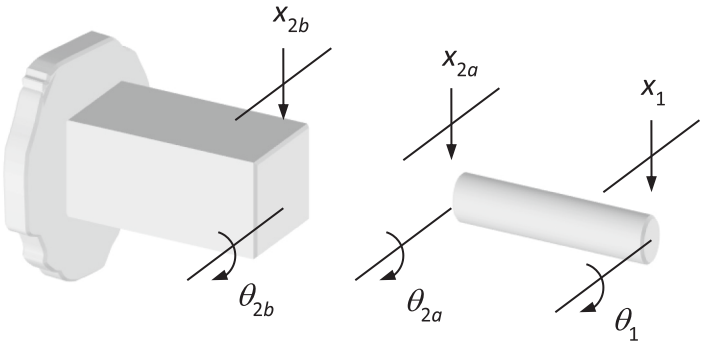

Fig. 5. Cylinder and prismatic cantilever beam components for RCSA example.

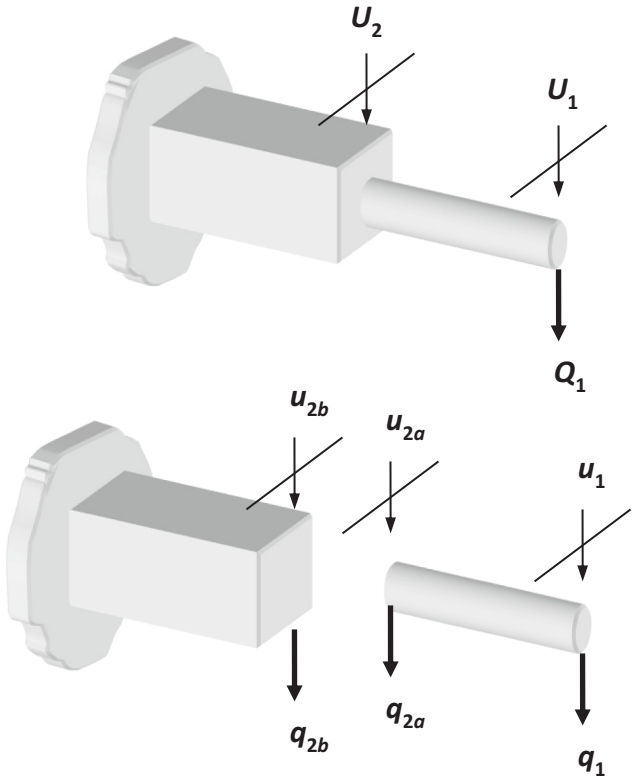

Fig. 6. Receptance coupling model for determining $\boldsymbol{G_{11}}$ using a rigid connection. (Top) assembly. (Bottom) components.

$$h_{2a1} = \frac{x_{2a}}{f_1} \qquad l_{2a1} = \frac{x_{2a}}{m_1} \qquad n_{2a1} = \frac{\theta_{2a}}{f_1} \qquad p_{2a1} = \frac{\theta_{2a}}{m_1} \tag{9}$$

Similarly, for the prismatic cantilever beam, the direct receptances at the coupling location 2*b* are given by Eq. (10).

$$h_{2b2b} = \frac{x_{2b}}{f_{2b}} \qquad l_{2b2b} = \frac{x_{2b}}{m_{2b}} \qquad n_{2b2b} = \frac{\theta_{2b}}{f_{2b}} \qquad p_{2b2b} = \frac{\theta_{2b}}{m_{2b}} \tag{10}$$

To simplify notation, the component receptances may be represented in matrix form as shown in Eqs. (11) through (14) for the cylinder and Eq. (15) for the prismatic cantilever beam. In Eqs. (11)–(15) R_{ij} is the generalized receptance matrix that describes both translational and rotational component behavior and u_i and q_j are the corresponding generalized displacement/rotation and force/couple vectors.

$$\begin{Bmatrix} x_1 \\ \theta_1 \end{Bmatrix} = \begin{bmatrix} h_{11} & l_{11} \\ n_{11} & p_{11} \end{bmatrix} \begin{Bmatrix} f_1 \\ m_1 \end{Bmatrix} \text{ or } \{\boldsymbol{u_1}\} = [\boldsymbol{R_{11}}]\{\boldsymbol{q_1}\} \tag{11}$$

$$\begin{Bmatrix} x_{2a} \\ \theta_{2a} \end{Bmatrix} = \begin{bmatrix} h_{2a2a} & l_{2a2a} \\ n_{2a2a} & p_{2a2a} \end{bmatrix} \begin{Bmatrix} f_{2a} \\ m_{2a} \end{Bmatrix} \text{ or } \{\boldsymbol{u_{2a}}\} = [\boldsymbol{R_{2a2a}}]\{\boldsymbol{q_{2a}}\} \tag{12}$$

$$\begin{Bmatrix} x_1 \\ \theta_1 \end{Bmatrix} = \begin{bmatrix} h_{12a} & l_{12a} \\ n_{12a} & p_{12a} \end{bmatrix} \begin{Bmatrix} f_{2a} \\ m_{2a} \end{Bmatrix} \text{ or } \{\boldsymbol{u_1}\} = [\boldsymbol{R_{12a}}]\{\boldsymbol{q_{2a}}\} \tag{13}$$

$$\begin{Bmatrix} x_{2a} \\ \theta_{2a} \end{Bmatrix} = \begin{bmatrix} h_{2a1} & l_{2a1} \\ n_{2a1} & p_{2a1} \end{bmatrix} \begin{Bmatrix} f_1 \\ m_1 \end{Bmatrix} \text{ or } \{\boldsymbol{u_{2a}}\} = [\boldsymbol{R_{2a1}}]\{\boldsymbol{q_1}\} \tag{14}$$

$$\begin{Bmatrix} x_{2b} \\ \theta_{2b} \end{Bmatrix} = \begin{bmatrix} h_{2b2b} & l_{2b2b} \\ n_{2b2b} & p_{2b2b} \end{bmatrix} \begin{Bmatrix} f_{2b} \\ m_{2b} \end{Bmatrix} \text{ or } \{\boldsymbol{u_{2b}}\} = [\boldsymbol{R_{2b2b}}]\{\boldsymbol{q_{2b}}\} \tag{15}$$

The component receptances are written using the generalized notation: $\boldsymbol{u_1} = \boldsymbol{R_{11}q_1} + \boldsymbol{R_{12a}q_{2a}}$ and $\boldsymbol{u_{2a}} = \boldsymbol{R_{2a1}q_1} + \boldsymbol{R_{2a2a}q_{2a}}$ for the cylinder and $\boldsymbol{u_{2b}} = \boldsymbol{R_{2b2b}q_{2b}}$ for the prismatic cantilever beam. For a rigid connection between the two components, the compatibility condition is $\boldsymbol{u_{2b}} - \boldsymbol{u_{2a}} = 0$. This indicates there is no relative motion at the coupling location. Additionally, if the component and assembly coordinates are at the same physical locations, then $\boldsymbol{u_1} = \boldsymbol{U_1}$ and $\boldsymbol{u_{2a}} = \boldsymbol{u_{2b}} = \boldsymbol{U_2}$ (due to the rigid coupling). The assembly receptances are written as shown in Eq. (16), which again incorporates the generalized notation.

$$\begin{Bmatrix} \boldsymbol{U_1} \\ \boldsymbol{U_2} \end{Bmatrix} = \begin{bmatrix} \boldsymbol{G_{11}} & \boldsymbol{G_{12}} \\ \boldsymbol{G_{21}} & \boldsymbol{G_{22}} \end{bmatrix} \begin{Bmatrix} \boldsymbol{Q_1} \\ \boldsymbol{Q_2} \end{Bmatrix}, \text{where } \boldsymbol{U}_i = \begin{Bmatrix} X_i \\ \Theta_i \end{Bmatrix}, \boldsymbol{G}_{ij} = \begin{bmatrix} H_{ij} & L_{ij} \\ N_{ij} & P_{ij} \end{bmatrix}, \text{and } \boldsymbol{Q}_j = \begin{Bmatrix} F_j \\ M_j \end{Bmatrix} \tag{16}$$

To determine the four assembly receptances at the free end of the cylinder, $\boldsymbol{G_{11}}$, the generalized force $\boldsymbol{Q_1}$ is applied to assembly coordinate $\boldsymbol{U_1}$ as shown in Fig. 6, where the generalized U_i and u_i vectors are shown schematically as "displacements", although they describe both transverse deflection and rotation. The associated equilibrium conditions are $\boldsymbol{q_{2a}} + \boldsymbol{q_{2b}} = 0$ (i.e., the internal forces/couples are balanced) and $\boldsymbol{q_1} = \boldsymbol{Q_1}$ (because the component and assembly generalized forces are located at the same spatial location).

By substituting the component displacements/rotations and equilibrium conditions into the compatibility condition, the expression for $\boldsymbol{q_{2b}}$ shown in Eq. (17) is obtained. The component force $\boldsymbol{q_{2a}}$ is then determined from the equilibrium condition $\boldsymbol{q_{2a}} = -\boldsymbol{q_{2b}}$.

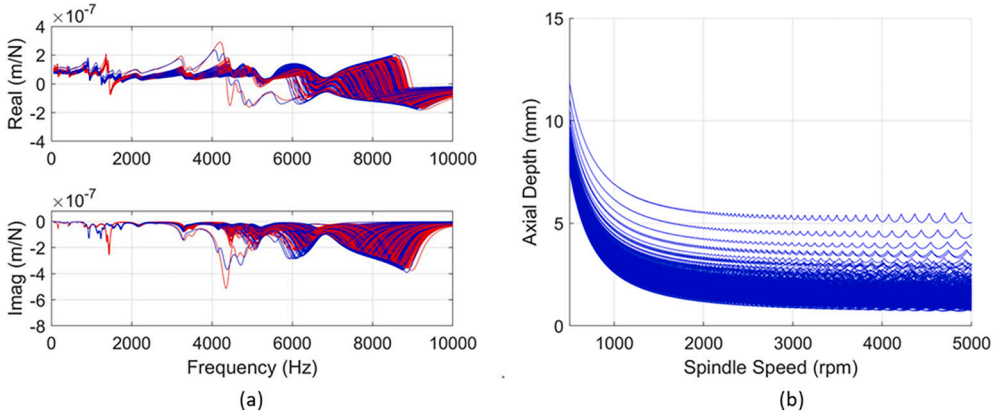

Fig. 7. (a) Tool tip FRFs predicted by RCSA for the *x* (red) and *y* (blue) directions including connection parameter uncertainty (*k* and *c*). (b) Stability limits calculated using the uncertain FRFs, uncertain force model coefficients (k_{tc} and k_{nc}), and process damping effects. (For interpretation of the references to color in this figure legend, the reader is referred to the web version of this article.)

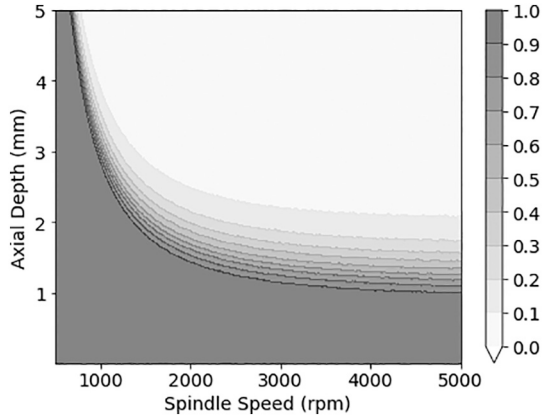

Fig. 8. Prior probability of stability for 304 stainless steel using the physics-informed method.

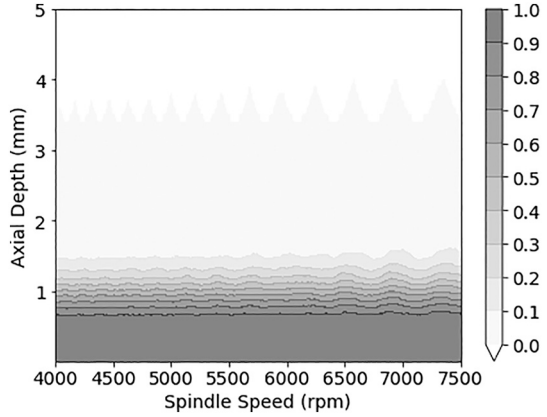

Fig. 9. Prior probability of stability for 6061-T6 aluminum using the physics-informed method.

$$\begin{aligned} &\boldsymbol{u}_{2b} - \mathrm{u}_{2a} = 0 \\ &\boldsymbol{R}_{2b2b}\boldsymbol{q}_{2b} - \boldsymbol{R}_{2a1}\boldsymbol{q}_1 - \boldsymbol{R}_{2a2a}\boldsymbol{q}_{2a} = 0 \\ &(\boldsymbol{R}_{2a2a} + \boldsymbol{R}_{2b2b})\boldsymbol{q}_{2b} - \boldsymbol{R}_{2a1}\boldsymbol{Q}_1 = 0 \\ &\boldsymbol{q}_{2b} = (\boldsymbol{R}_{2a2a} + \boldsymbol{R}_{2b2b})^{-1}\boldsymbol{R}_{2a1}\boldsymbol{Q}_1 \end{aligned} \tag{17}$$

The expression for $\boldsymbol{G_{11}}$ is given by Eq. (18). The (1, 1) location, H_{11}, in the 2 × 2 matrix, $\boldsymbol{G_{11}}$, is the displacement-to-force receptance required for milling stability prediction.

$$\boldsymbol{G}_{11} = \frac{\boldsymbol{U}_1}{\boldsymbol{Q}_1} = \frac{\boldsymbol{u}_1}{\boldsymbol{Q}_1} = \frac{\boldsymbol{R}_{11}\boldsymbol{q}_1 + \boldsymbol{R}_{12a}\boldsymbol{q}_{2a}}{\boldsymbol{Q}_1} = \frac{\boldsymbol{R}_{11}\boldsymbol{Q}_1 - \boldsymbol{R}_{12a}(\boldsymbol{R}_{2a2a} + \boldsymbol{R}_{2b2b})^{-1}\boldsymbol{R}_{2a1}\boldsymbol{Q}_1}{\boldsymbol{Q}_1}$$

$$\boldsymbol{G}_{11} = \boldsymbol{R}_{11} - \boldsymbol{R}_{12a}(\boldsymbol{R}_{2a2a} + \boldsymbol{R}_{2b2b})^{-1}\boldsymbol{R}_{2a1} = \begin{bmatrix} H_{11} & L_{11} \\ N_{11} & P_{11} \end{bmatrix} \tag{18}$$

For a non-rigid coupling with energy dissipation (damping) between the tool and holder, Eq. (19) is modified to include a connection stiffness matrix, [$\boldsymbol{K}$], as shown in Eq. (18).

$$\boldsymbol{G}_{11} = \boldsymbol{R}_{11} - \boldsymbol{R}_{12a}\left(\boldsymbol{R}_{2a2a} + \boldsymbol{R}_{2b2b} + \boldsymbol{K}^{-1}\right)^{-1}\boldsymbol{R}_{2a1} = \begin{bmatrix} H_{11} & L_{11} \\ N_{11} & P_{11} \end{bmatrix} \tag{19}$$

The complex-valued, frequency-dependent connection stiffness matrix is defined in Eq. (20), where k indicates stiffness, c represents viscous damping, and ω is frequency.

$$[\boldsymbol{K}] = \begin{bmatrix} 0 & k + i\omega c \\ k + i\omega c & 0 \end{bmatrix} \tag{20}$$

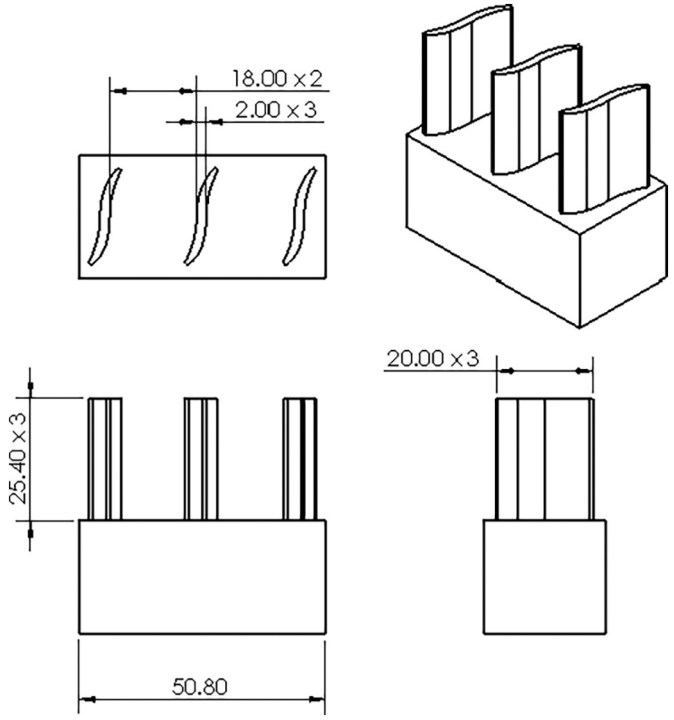

Fig. 10. IBR geometry (dimensions in mm).

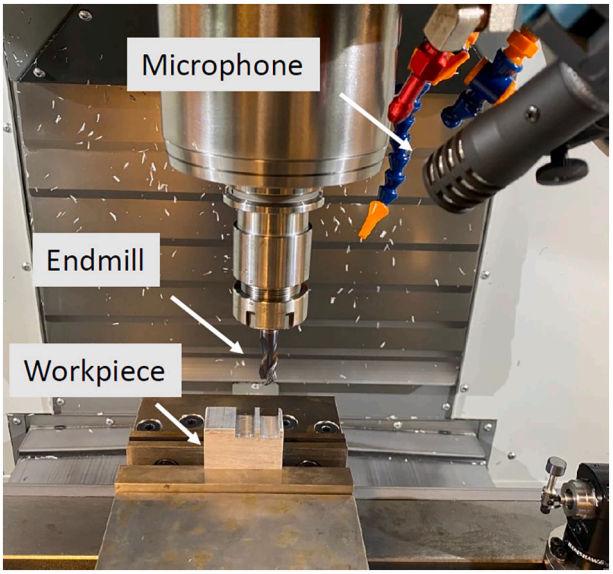

Fig. 11. Experimental setup for stability testing.

2.5. Physics-informed Bayesian machine learning (PIBML)

A physics-informed prior was generated by propagating uncertainties in the stability model inputs (k_{tc} and k_{nc} from Eqs. (3) and (4), k and c from Eq. (20)) to uncertainty in the stability limit using Monte Carlo simulation. In each iteration, a random sample was selected from the {k_{tc}, k_{nc}, k, c} normal distributions. For k_{tc} and k_{nc}, the standard deviations were 25 % of the mean values from Table 1. The 25 % value was based on the authors' experience in using orthogonal turning finite element simulations for the coefficient determination. For example, smaller uncertainty values may be chosen if the force coefficients are determined using experimental results. For k and c, the mean values were 6 × 10^6 N/rad and 26 N-s/rad (based on prior modeling efforts for

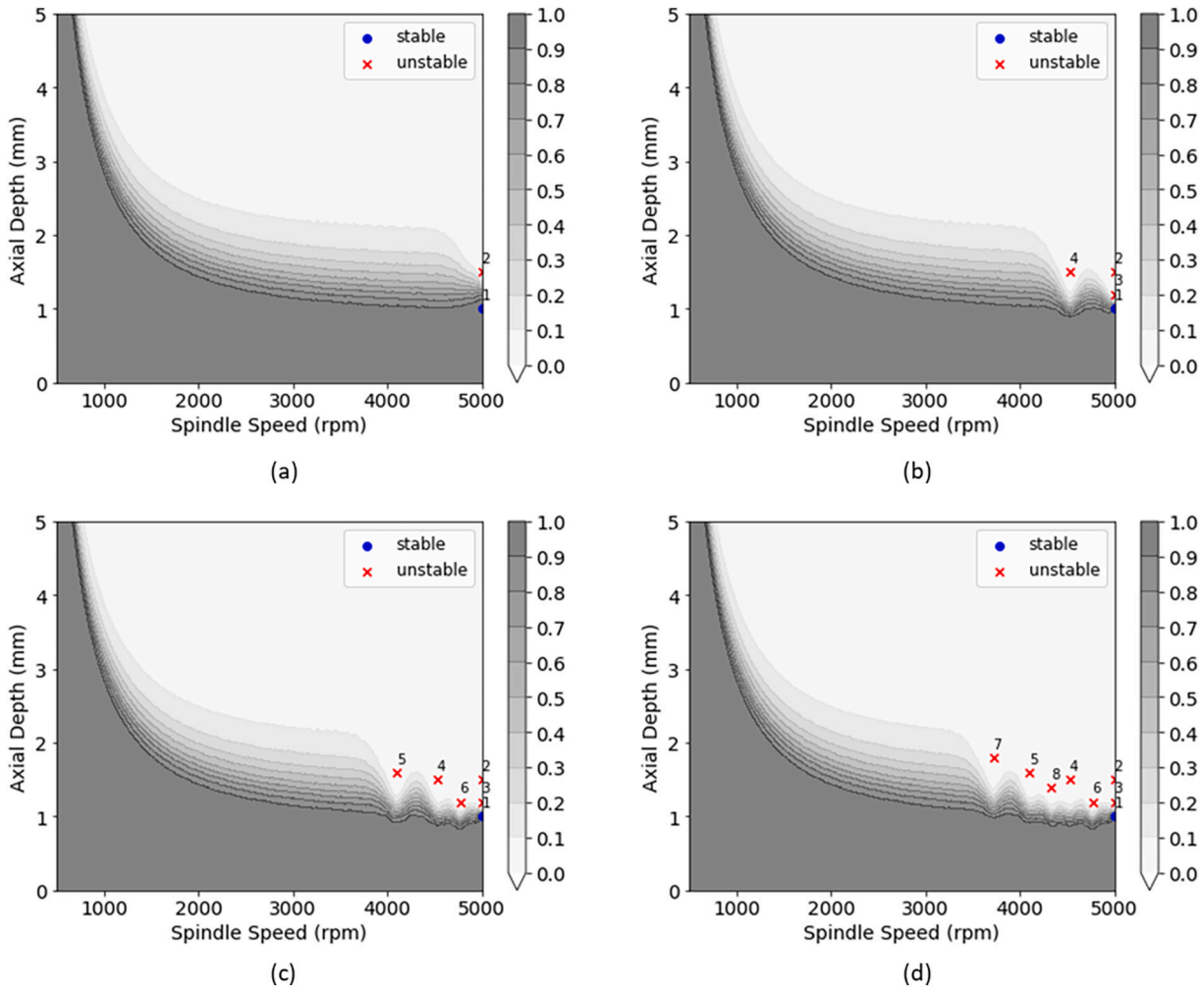

Fig. 12. Posterior probability of stability for 304 stainless steel. (a) Two tests. (b) Four tests. (c) Six tests. (d) Seven tests. The optimal parameters {5000 rpm, 1.0 mm} were identified in seven tests using the maximum expected improvement in *MRR* criterion.

ER32 collet holders). The standard deviations were again 25 % of the mean values. The stability limit was then calculated using these inputs. Fig. 7 displays the variation in tool tip FRFs in the x (feed) and y directions and corresponding distribution in stability limits for slotting in 304 stainless steel, where process damping is included using Eq. (5). Fig. 7 shows 500 stability samples for 304 stainless steel.

The spindle speed-axial depth of cut domain was divided into a grid of points. At each grid point, the prior probability of stability was determined by calculating the fraction of the number of stability boundaries where the predicted stable axial depth is greater than the grid point axial depth at the same spindle speed. This is shown in Eq. (21). The prior probability of stability was used in the PIBML approach to calculate the posterior probability of stability after new information was obtained from test results.

$$p(s_g) = \frac{1}{N}\sum_{i=1}^{N} b_g < b_{lim_i} \tag{21}$$

In Eq. (21), $p(s_g)$ is the prior probability of stability at a selected grid point, N is the total number of stability samples, b_g is the selected axial depth at grid point g, and b_{lim} is the limiting axial depth of cut at the selected spindle speed, denoted by Ω_g. To illustrate, all 500 stability samples shown in Fig. 7 predict stable conditions at {5000 rpm, 0.2 mm}. Therefore, the prior probability of stability at {5000 rpm, 0.2 mm} is 1. The prior probability of stability is 0 at {5000 rpm, 5.1 mm} since all stability samples predict {5000 rpm, 5.1 mm} as unstable. The probability of stability at all intermediate axial depths of cut at 5000 rpm can be calculated using Eq. (21). Fig. 8 shows the prior probability of stability for 304 stainless steel. Fig. 9 shows the prior probability of stability for 6061-T6 aluminum calculated using the same procedure. Note that the spindle speed range for 6061-T6 aluminum is higher than 304 stainless steel.

3. Results

3.1. Experimental setup

Fig. 10 shows the selected IBR geometry. Three blades were machined to represent an IBR. Fig. 11 shows the experimental setup. The cuts were recorded using a microphone to determine the stability.

3.2. 304 stainless steel IBR

The manufacturer recommended an axial depth of 6.35 mm and spindle speed range of 2215 rpm to 2674 rpm for slotting. The recommended axial depth was predicted to be unstable for all spindle speeds according to the prior probability of stability (see Fig. 8). Testing was completed to identify optimal stable machining parameters. Because the stability limit is lowest for slotting, this radial depth dictated the axial depth for each layer (the blades were fully machined one axial layer at a time from tip to root). Testing was therefore performed at slotting conditions to identify the optimal stable machining parameters. The test

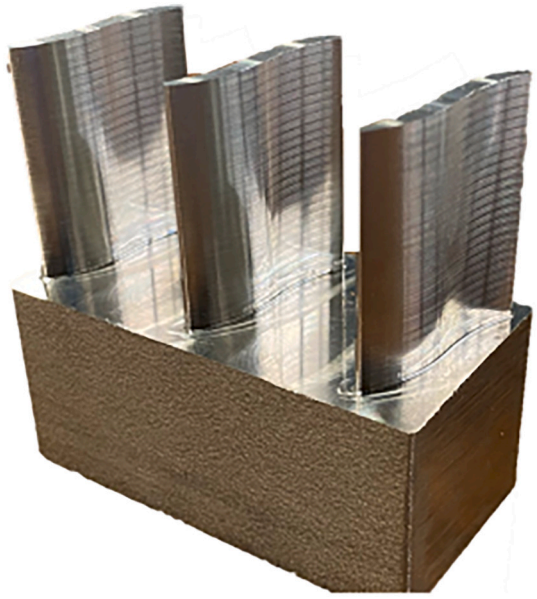

Fig. 13. Final machined 304 stainless steel IBR using optimal stable parameters {5000 rpm, 1 mm}. Note that the manufacturer recommended spindle speed range of 2215 rpm to 2674 rpm and 6.35 axial depth of cut for slotting was unstable.

parameters were selected using the maximum expected improvement in *MRR* criterion (shown in Eq. (2)). The spindle speed and axial depth of cut range were divided into gird points with 10 rpm and 0.1 mm spacing, respectively. The test procedure follows.

1. Calculate the expected improvement in material removal rate (Eq. (2)) at all grid points using the prior probability of stability. The prior probability of stability for 304 stainless steel is shown in Fig. 8.
2. Select test spindle speed and axial depth where the expected material removal rate is maximum.
3. Complete the test at slotting conditions and record the audio signal using a microphone.
4. Determine the cut stability using the ratio of the tooth passing frequency and chatter frequency.
5. Update the prior probability of stability using the Bayesian learning method described in [14] to calculate the posterior probability of stability.
6. Repeat steps 1–5 until the maximum expected improvement in *MRR* is less than 5 %.

The feed per tooth was selected as 0.06 mm/tooth. The spindle speed range was selected as 500 rpm to 5000 rpm and the axial depth of cut range was 0 mm to 5 mm. The maximum spindle speed was limited to 5000 rpm to provide adequate tool life for machining the entire IBR with a single endmill. Fig. 12 shows the posterior probability of stability after multiple tests. Using the physics-informed prior, seven test cuts were required for the PIBML model to identify the optimal combination of {5000 rpm, 1.0 mm}. The identified optimal stable parameters were used to machine the IBR geometry shown in Fig. 10. The final machined IBR is shown in Fig. 13. The stable parameters resulted in a good surface finish with no chatter marks. Note that the procedure described in this paper applies to roughing of IBR from a prismatic stock. Therefore, a quantitative assessment of surface finish and blade dimensions was not

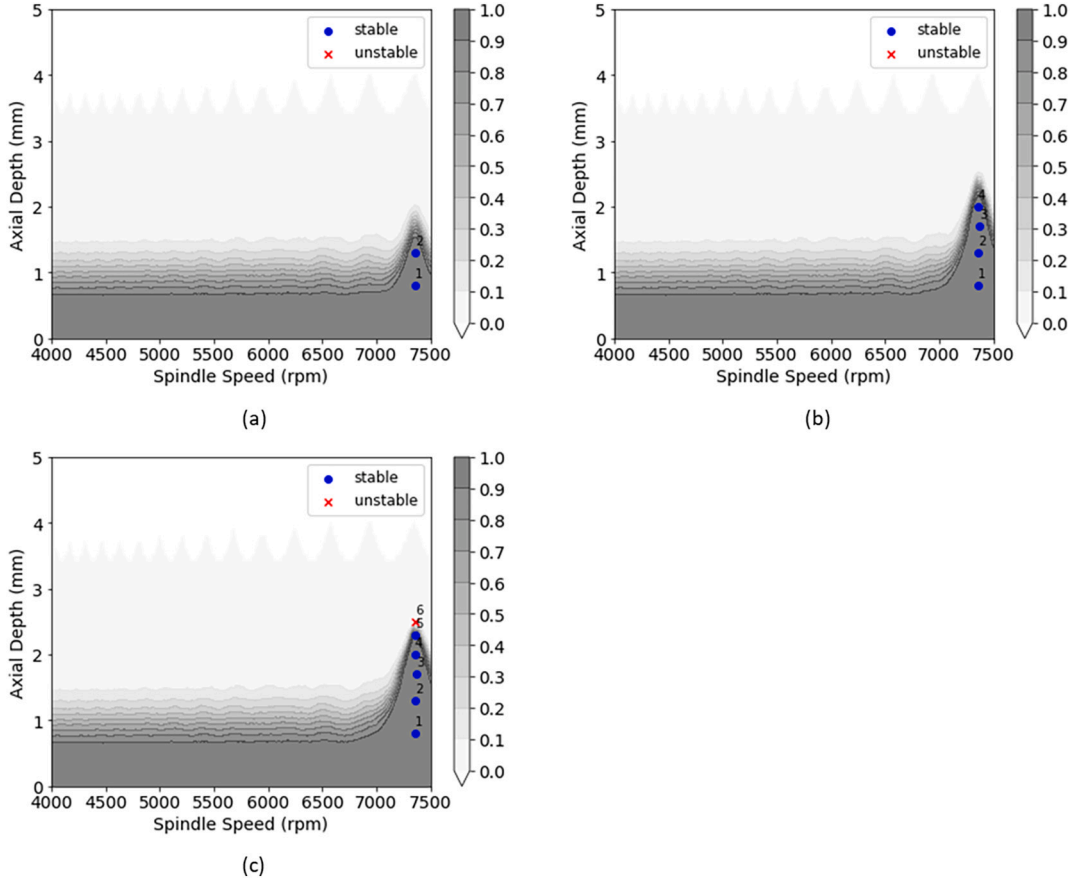

Fig. 14. Posterior probability of stability for 6061-T6 aluminum. (a) Two tests. (b) 4 tests; and (c) 6 tests. The optimal parameters {7360 rpm, 2.3 mm} were identified in six tests using the maximum expected improvement in *MRR* criterion.

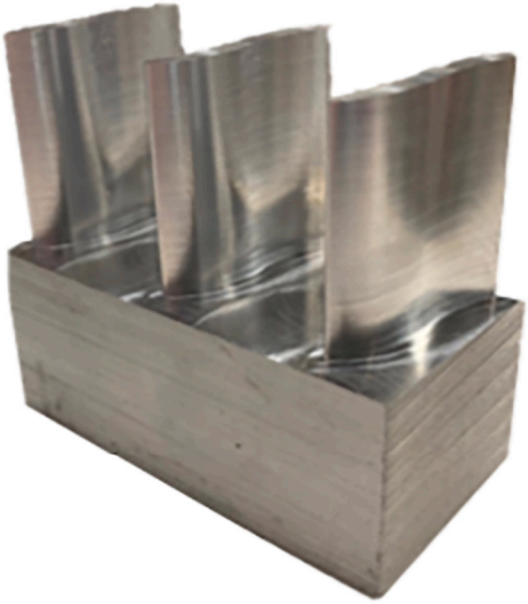

Fig. 15. Final machined 6061-T6 aluminum IBR using optimal stable parameters {7360 rpm, 2.3 mm}. Note that the manufacturer recommended spindle speed range of 6264 rpm to 24,828 and 6.35 axial depth of cut for slotting was unstable.

completed.

To mimic industrial rough machining operations, the toolpath was optimized using Third Wave Systems Production Module™ feedrate scheduling software [42]. The feedrate scheduling approach modifies the feedrate throughout the tool path, resulting in a user-defined constant force. This provided a 15 % cycle time reduction relative to the original CAM tool path. Details on the Production Module™ feedrate scheduling software are provided in [42]. Note that modifying the feedrate does not influence the stability of the optimal parameters to first order.

3.3. 6061-T6 aluminum IBR

For 6061-T6 aluminum, the endmill manufacturer recommended an axial depth of 6.35 mm and a spindle speed range from 6264 rpm to 24,828 rpm for slotting. This axial depth was predicted to be unstable for all spindle speeds according to the prior shown in Fig. 9. As noted, since the stability limit is lowest for slotting, this radial depth dictated the axial depth for each layer. Testing was completed using the procedure described in Section 3.2. The spindle speed-axial depth of cut domain was divided into a grid of points with 10 rpm and 0.1 mm spacing, respectively. The feed per tooth was selected as 0.1 mm/tooth. The spindle speed range was selected as 4000 rpm to 7500 rpm and the axial depth of cut range was 0 mm to 5 mm. Fig. 14 shows the posterior probability of stability after two, four, and six tests. Using the physics-informed prior, six test cuts were required for the PIBML model to converge to the optimal combination of {7360 rpm, 2.3 mm}. Recall that testing was terminated when the maximum expected improvement in *MRR* is less than 5 %. The optimal stable parameters were used to machine the IBR geometry shown in Fig. 10. The final machined IBR is shown in Fig. 15. Like the 304 stainless steel IBR, the stable parameters resulted in a good surface finish with no chatter marks. The application of the feedrate scheduling approach using Production Module™ [42] on the toolpath resulted in a time reduction of 35 % versus the original toolpath from the CAM software.

4. Discussion

This paper described a physics-informed approach to select the prior in Bayesian machine learning. In the absence of information on the frequency response function and cutting force coefficients, an uninformed prior that only uses the knowledge that it is more likely to obtain an unstable cut at higher axial depths of cut may be selected [14]. The uninformed prior is defined by assuming that the probability of stability linearly decreases from 1 at 0 mm axial depth to 0.05 (near zero) at the maximum axial depth of cut; see Fig. 1(a). In this section, the efficiency of the physics-informed approach is demonstrated by comparison with the uninformed prior.

Fig. 16 shows the results for 304 stainless steel starting with an uninformed prior. Fig. 16(a) shows the uninformed prior. Fig. 16(b) displays the posterior probability of stability and the test sequence. The procedure to identify the optimal stable parameters described in Section 3.2 was applied to select the test parameters starting with the uninformed prior. The optimal stable parameters identified were {4680 rpm, 1 mm} after 25 tests using the maximum expected reduction in *MRR* criterion. For 304 stainless steel, starting with an uninformed prior resulted in 18 more tests (25 compared to seven with a physics-informed prior) and a 6.4 % reduction in the optimal *MRR*. Furthermore, after the first stable result is identified at {4680 rpm, 1 mm} at test 12, the maximum expected reduction in *MRR* criterion recommends successively higher axial depths of cut. This can result in multiple unstable cuts during testing (as seen from test 14 to test 24), which may damage the tool and spindle.

Fig. 17 shows the results for 6061-T6 aluminum. Fig. 17(a) shows the

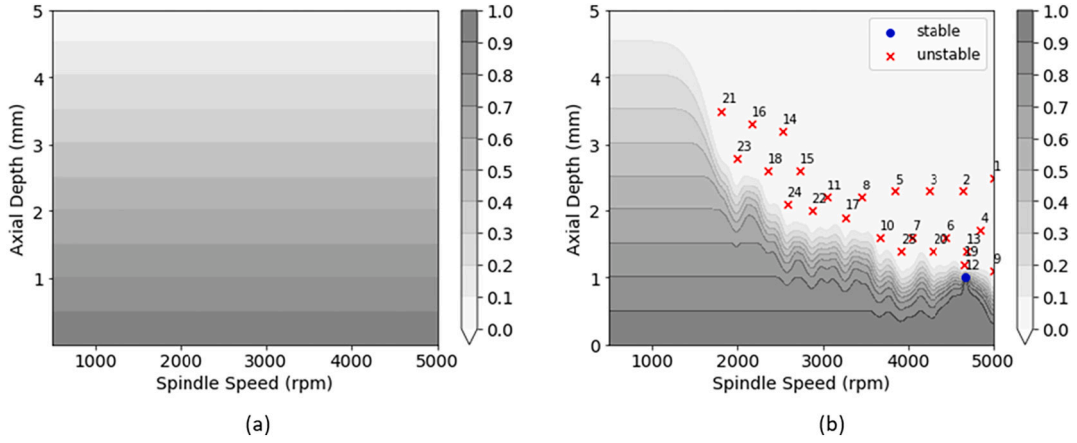

Fig. 16. (a) Uninformed prior assuming a linear decrease in probability of stability with axial depth for 304 stainless steel. (b) Posterior probability of stability after 25 tests. The optimal stable parameters were {4680 rpm, 1 mm} identified at test 12.

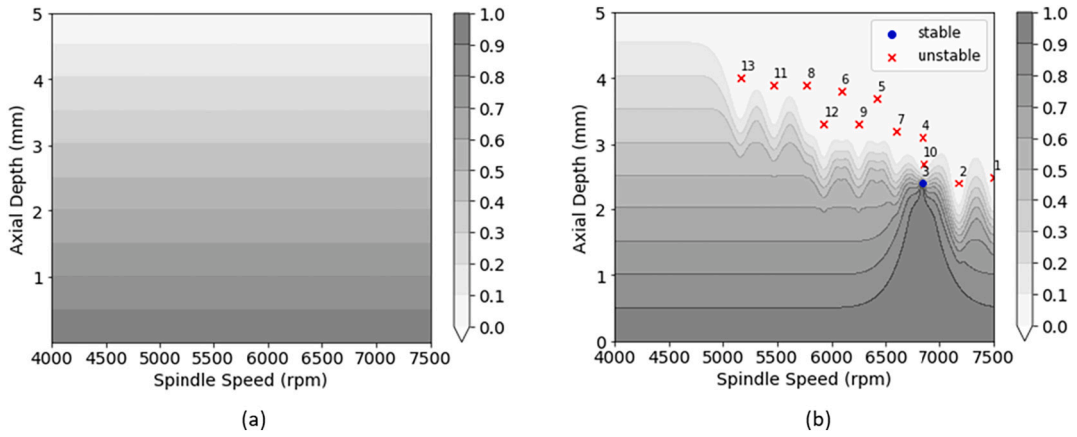

Fig. 17. (a) Uninformed prior assuming a linear decrease in the probability of stability with axial depth for 6061-T6 aluminum. (b) Posterior probability of stability after 13 tests. The optimal stable parameters were {6840 rpm, 2.4 mm} identified at test 3.

uninformed prior. Fig. 17(b) displays the posterior probability of stability and the test sequence. The optimal stable parameters identified were {6840 rpm, 2.4 mm} after 13 tests using the maximum expected reduction in *MRR* criterion. For 6061-T6 aluminum, starting with an uninformed prior resulted in seven more tests (13 compared to six with a physics-informed prior) and a 7.0 % reduction in the optimal *MRR*.

As shown in Figs. 16 and 17, the physics-informed prior results in a significant reduction in the number of tests required to identify the optimal stable parameters. The physics-informed approach described in this paper does not need extensive experimental tests for input data. The only experimental data needed is the artifact-spindle-machine FRF measurement, which can subsequently be used to model any tool-holder-spindle-machine combination using the RCSA approach. The cutting force coefficients were determined using a finite element approach and did not require experimental testing. Furthermore, user-defined uncertainties were included for the RCSA and finite element methods through Monte Carlo simulation to incorporate modeling uncertainties. Combining the physics-informed prior with the Bayesian learning approach results in rapid identification of the optimal stable machining parameters.

5. Conclusions

This paper described a physics-informed Bayesian machine learning (PIBML) approach that implemented three physics-based models: 1) an RCSA prediction for the tool tip FRFs; 2) finite element software prediction of the mechanistic force model coefficients; and 3) a spindle speed-dependent power law model for process damping in a Bayesian machine learning algorithm. Monte Carlo simulation was used to propagate uncertainty in the RCSA and force model physics-based inputs into uncertainty in the predicted stability limit. These uncertain stability limits were used to generate a probability of stability map that represented initial knowledge about milling stability, referred to as the prior.

The probabilistic prior was then compared to machining parameter recommendations provided by the endmill manufacturer. For both the 6061-T6 aluminum and 304 stainless steel workpiece material cases, the recommended axial depth of cut was predicted to be unstable over the full spindle speed range. Testing was therefore performed to update the prior and obtain the posterior probability of stability. The probabilistic posterior was used to select optimal machining parameters and the IBRs were machined using optimized tool paths. Machining trials confirmed stable machining performance. The disagreement between manufacturer recommendations and milling performance emphasizes the need for broad implementation of PIBML approaches, as demonstrated here, to increase machining productivity and efficiency.

Declaration of competing interest

The authors declare that they have no known competing financial interests or personal relationships that could have appeared to influence the work reported in this paper.

Acknowledgments

This research was supported by MxD project number 20-11-04 Physics-Guided Machine Learning (PGML) for CNC Milling. This material is based on research sponsored by Office of the Under Secretary of Defense for Research and Engineering, Strategic Technology Protection and Exploitation, Defense Manufacturing Science and Technology Program under agreement number W15QKN-19-3-0003 between MxD and the Government. The U.S. Government is authorized to reproduce and distribute reprints for Governmental purposes.

References

[1] https://www.thomasnet.com/insights/cnc-machining-projected-to-be-100b-industry-by-2025/ (n.d.).
[2] Schmitz TL, Smith KS. Machining dynamics: frequency response to improved productivity. 2nd Ed. New York, NY: Springer; 2019.
[3] Altintas Y, Budak E. Analytical prediction of stability lobes in milling. Ann CIRP 1995;44(1):357–62.
[4] Davies MA, Dutterer BS, Pratt JR, Schaut AJ. On the dynamics of high-speed milling with long, slender endmills. Ann CIRP 1998;47(1):55–60.
[5] Davies MA, Pratt JR, Dutterer BS, Burns TJ. The stability of low radial immersion milling. Ann CIRP 2000;49(1):37–40.
[6] Insperger T, Stépán G. Updated semi-discretization method for periodic delay-differential equations with discrete delay. Int J Num Methods Eng 1995;61(1):117–41.
[7] Bayly PV, Halley JE, Mann BP, Davies MA. Stability of interrupted cutting by temporal finite element analysis. J Manuf Sci Eng 2003;125(2):220–5.
[8] Cherukuri H, Perez-Bernabeu E, Selles M, Schmitz T. Machining chatter prediction using a data learning model. J Manuf Matl.Proc 2019;3(2):45.
[9] Denkena B, Bergmann B, Reimer S. Analysis of different machine learning algorithms to learn stability lobe diagrams. Procedia CIRP 2020;88:282–7.
[10] Bergmann B, Reimer S. Online adaption of milling parameters for a stable and productive process. CIRP Ann 2021;70(1):341–4.
[11] Postel M, Bugdayci B, Wegener K. Ensemble transfer learning for refining stability predictions in milling using experimental stability states. Int J Adv Manuf Technol 2020;107(9):4123–39.
[12] Chen G, Li Y, Liu X, Yang B. Physics-informed Bayesian inference for milling stability analysis. Int J Mach Tools Manuf 2021;167:103767.
[13] Li K, He S, Liu H, Mao X, Li B, Luo B. Bayesian uncertainty quantification and propagation for prediction of milling stability lobe. Mech Syst Signal Proc 2020;138:106532.
[14] Karandikar J, Honeycutt A, Schmitz T, Smith S. Stability boundary and optimal operating parameter identification in milling using Bayesian learning. J Manuf Proc 2020;56:1252–62.
[15] Cornelius A, Karandikar J, Gomez M, Schmitz T. A bayesian framework for milling stability prediction and reverse parameter identification. Procedia Manuf 2021;53:760–72.

[16] Karandikar J, Honeycutt A, Smith S, Schmitz T. Milling stability identification using bayesian machine learning. Procedia CIRP 2020;93:1423–8.
[17] Schmitz T, Donaldson RR. Predicting high-speed machining dynamics by substructure analysis. CIRP Ann 2000;49(1):303–8.
[18] Schmitz T, Duncan GS. Three-component receptance coupling substructure analysis for tool point dynamics prediction. J Manuf Sci Eng 2005;127(4):781–90.
[19] https://thirdwavesys.com/machining-modeling/advantedge/ (n.d.).
[20] Wallace PW, Andrew C. Machining forces: some effects of tool vibration. J Mech Eng Sci 1965;7(2):152–62.
[21] Sisson TR, Kegg RL. An explanation of low-speed chatter effects. J Eng For Ind 1969;91:951–8.
[22] Peters J, Vanherck P, Van Brussel H. The measurement of the dynamic cutting coefficient. CIRP Ann 1981;21(2):129–36.
[23] Tlusty J. Analysis of the state of research in cutting dynamics. CIRP Ann 1978;27 (2):583–9.
[24] Wu DW. A new approach of formulating the transfer function for dynamic cutting processes. J Eng For Ind 1989;111:37–47.
[25] Elbestawi MA, Ismail F, Du R, Ullagaddi BC. Modelling machining dynamics damping in the tool-workpiece interface. J Eng For Ind 1994;116:435–9.
[26] Lee BY, Tarng YS, Ma SC. Modeling of the process damping force in chatter vibration. Int J Mach Tools Manuf 1995;35(7):951–62.
[27] Abrari F, Elbestawi MA, Spence AD. On the dynamics of ball end milling: modeling of cutting forces and stability analysis. Int J Mach Tools Manuf 1998;38(3):215–37.
[28] Ahmadi K, Ismail F. Machining chatter in flank milling. Int J Mach Tools Manuf 2010;50(1):75–85.
[29] Huang CY, Wang JJ. Mechanistic modeling of process damping in peripheral milling. J Manuf Sci Eng 2007;129:12–20.
[30] Chiou YS, Chung ES, Liang SY. Analysis of tool wear effect on chatter stability in turning. Int J Mech Sci 1995;37(4):391–404.
[31] Chiou RY, Liang SY. Chatter stability of a slender cutting tool in turning with tool wear effect. Int J Mach Tools Manuf 1998;38(4):315–27.
[32] Chandiramani NK, Pothala T. Dynamics of 2-dof regenerative chatter during turning. J Sound Vib 2006;290(1–2):448–64.
[33] Jemielniak K, Widota A. Numerical simulation of non-linear chatter vibration in turning. Int J Mach Tools Manuf 1989;29(2):239–47.
[34] Ahmadi K, Ismail F. Experimental investigation of process damping nonlinearity in machining chatter. Int J Mach Tools Manuf 2010;50(11):1006–14.
[35] Budak E, Tunc LT. A new method for identification and modeling of process damping in machining. J Manuf Sci Eng. 2009;131(051019):1–10.
[36] Altintas Y, Eynian M, Onozuka H. Identification of dynamic cutting force coefficients and chatter stability with process damping. CIRP Ann 2008;57(1): 371–4.
[37] Tyler C, Schmitz T. Process damping analytical stability analysis and validation. Trans. of NAMRI/SME 2012;40.
[38] Tyler C, Karandikar J, Schmitz T. Process damping coefficient identification using Bayesian inference. Trans NAMRI/SME 2013;41.
[39] Tyler CT, Schmitz TL. Analytical process damping stability prediction. J Manuf Proc 2013;15(1):69–76.
[40] Tyler C, Troutman J, Schmitz T. Radial depth of cut stability lobe diagrams with process damping effects. Precis Eng 2015;40:318–24.
[41] Weaver Jr W, Timoshenko S, Young D. Vibration problems in engineering. 5th Ed. New York, NY: John Wiley and Sons; 1990.
[42] https://thirdwavesys.com/machining-modeling/productionmodule/ (n.d.).